# Reconstructing Farallon Plate Subduction Beneath North America Back to the Late Cretaceous

Lijun Liu, *et al.*

*Science* **322**, 934 (2008);
DOI: 10.1126/science.1162921



*Science* (print ISSN 0036-8075; online ISSN 1095-9203) is published weekly, except the last week in December, by the American Association for the Advancement of Science, 1200 New York Avenue NW, Washington, DC 20005. 

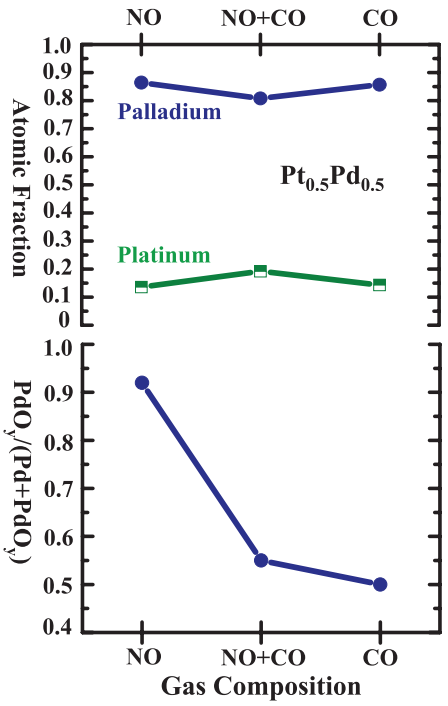


**Fig. 3.** (**Top**) Evolution of the Pd and Pt atomic fractions in $Pt_{0.5}Pd_{0.5}$ NPs at 300°C under oxidizing (100 mtorr NO), catalytic (100 mtorr NO and 100 mtorr CO), and reducing (100 mtorr CO) conditions. The *x* axis represents the different gas environments. (**Bottom**) Evolution of the atomic fraction of the oxidized Pd atoms in the examined region under the same reaction conditions as the top panel. All atomic fractions were obtained at an x-ray energy of 350 eV for Pt4f (KE ~280 eV) and 630 eV for Pd3d (KE ~ 280 eV). The *y*-axis error in the data is ±0.03.

similar to that formed in pure CO [fig. S3 (*11*)]. When Al Kα x-rays at 1486.6 eV were used, the Rh fraction in the $Rh_{0.5}Pd_{0.5}$ NPs measured in UHV after alternating oxidizing and reducing reactions [fig. S4 (*11*)] was 0.36 ± 0.03, much lower than the 0.52 ± 0.03 value of the as-synthesized NPs before reaction also measured in UHV with Al Kα x-rays (Fig. 1A). This difference indicates that the core region (at depth greater than 1.6 nm) also participates in the restructuring of the NPs.

The opposite segregation behavior of Rh and Pd under oxidizing and reducing conditions can be explained by considering the surface energy in the metals and in the oxides. The lower surface energy of Pd relative to Rh tends to drive Pd metal atoms to the surface (*13*–*15*). The fact that the Rh oxide is more stable than the Pd oxide provides the driving force for the segregation and preferential oxidation of Rh at the surface (*16*). When a reducing gas, CO, is added to NO, the oxides are reduced to the metallic state and the oxygen atoms react with adsorbed CO to form $CO_2$ and desorb. Because of their higher surface free energy, the Rh atoms migrate to the core, thereby decreasing the atomic fraction of Rh in the shell under reducing and catalytic conditions.

In the $Pt_{0.5}Pd_{0.5}$ NPs, synthesized with the same procedure described in the SOM, the shell region is substantially richer in Pd. Pd has lower surface energy and is a more reactive metal than Pt (*15*, *16*). Under oxidizing conditions, it forms a shell with 92% $PdO_y$ without substantial segregation of Pt atoms as compared to the as-synthesized $Pt_{0.5}Pd_{0.5}$ NPs (Figs. 3 and 1B). During catalytic reaction and under reducing conditions, the $PdO_y$ is substantially reduced (bottom part of Fig. 3). There is no obvious segregation under these conditions. Compared to $Rh_{0.5}Pd_{0.5}$, however, the $Pt_{0.5}Pd_{0.5}$ NPs do not exhibit the strong segregation and reversibility characteristic of the $Rh_{0.5}Pd_{0.5}$ NPs as the gas composition changes sequentially from oxidizing, to catalytic, to reducing as shown in the top part of Fig. 3. Because Pt is much less easily oxidized (*16*) and has higher surface energy (*15*), the Pt atoms are not pinned to the surface by the formation of oxide. Thus, there is no substantial atomic reorganization in reactive environments.

The restructuring phenomenon observed in the bimetallic NPs induced by changes in reactive gas offers an interesting way of engineering the nanostructure of NPs for catalysis and other applications. One goal could be the synthesis of "smart" catalysts whose structure changes advantageously depending on the reaction environment. Our results suggest that the combination of a tunable colloid chemistry-based synthesis, followed by the controllable engineering of the structure of NPs with the use of reactive gases, opens a new door for designing new catalysts and shaping the catalytic properties of nanomaterials by structural engineering in reactive environments.

**References and Notes**

1. G. A. Somorjai, *Introduction to Surface Chemistry and Catalysis* (Wiley, New York, 1994), pp. 500–512.
2. G. W. Huber, J. W. Shabaker, J. A. Dumesic, *Science* **300**, 2075 (2003).
3. D. I. Enache *et al.*, *Science* **311**, 362 (2006).
4. F. Maroun, F. Ozanam, O. M. Magnussen, R. J. Behm, *Science* **293**, 1811 (2001).
5. C. Burda, X. Chen, R. Narayanan, M. A. El-Sayed, *Chem. Rev.* **105**, 1025 (2005).
6. A. Christensen, P. Stoltze, J. K. Norskov, *J. Phys. Condens. Matter* **7**, 1047 (1995).
7. C. T. Campbell, *Annu. Rev. Phys. Chem.* **41**, 775 (1990).
8. J. A. Rodriguez, D. W. Goodman, *Science* **257**, 897 (1992).
9. D. F. Ogletree *et al.*, *Rev. Sci. Instrum.* **73**, 3872 (2002).
10. M. Salmeron, R. Schlögl, *Surf. Sci. Rep.* **63**, 169 (2008).
11. Methods and additional data are available as supporting material on *Science* Online.
12. C. J. Powell, A. Jablonski, *NIST Electron Inelastic-Mean-Free-Path Database*, ed. 1.1 (National Institute of Standards and Technology, Gaithersburg, MD, 2000).
13. A. V. Ruban, H. L. Skriver, J. K. Norskov, *Phys. Rev. B* **59**, 15990 (1999).
14. T. Maillet, J. Barbier, P. Gelin, H. Praliaud, D. Duprez, *J. Catal.* **202**, 367 (2001).
15. H. L. Skriver, N. M. Rosengaard, *Phys. Rev. B* **46**, 7157 (1992).
16. M. Salmeron, L. Brewer, G. A. Somorjai, *Surf. Sci.* **112**, 207 (1981).
17. Supported by the director of the Office of Science; Office of Advanced Scientific Computing Research; Office of Basic Energy Sciences, Materials Sciences and Engineering; and Chemical Sciences, Geosciences, and Biosciences Division of the U.S. Department of Energy under contract DE-AC02-05CH11231.

**Supporting Online Material**

www.sciencemag.org/cgi/content/full/1164170/DC1
Materials and Methods
SOM Text
Figs. S1 to S5
References

4 August 2008; accepted 29 September 2008
Published online 9 October 2008;
10.1126/science.1164170
Include this information when citing this paper.

# Reconstructing Farallon Plate Subduction Beneath North America Back to the Late Cretaceous

**Lijun Liu,* Sonja Spasojević, Michael Gurnis**

Using an inverse mantle convection model that assimilates seismic structure and plate motions, we reconstruct Farallon plate subduction back to 100 million years ago. Models consistent with stratigraphy constrain the depth dependence of mantle viscosity and buoyancy, requiring that the Farallon slab was flat lying in the Late Cretaceous, consistent with geological reconstructions. The simulation predicts that an extensive zone of shallow-dipping subduction extended beyond the flat-lying slab farther east and north by up to 1000 kilometers. The limited region of flat subduction is consistent with the notion that subduction of an oceanic plateau caused the slab to flatten. The results imply that seismic images of the current mantle provide more constraints on past tectonic events than previously recognized.

Mantle convection is a time-dependent process, as evident through the evolution of plate motions, changes in the configuration of plate margins, and pulses of hotspot volcanism. How does convection actually change and what time-dependent models are consistent with the range of observational constraints? Answers to these questions are important because the time dependence of the system is strongly dependent on key uncertainties, including the depth dependence of mantle viscosity, the rheology and buoyancy of slabs, and the thermo-

dynamics of solid-solid phase transitions (*1*–*3*). Modeling past convection accurately enough to reveal causes of geological and current seismic data is difficult because forward models are strongly dependent on uncertain initial conditions such as the mantle's thermal structure. This ambiguity of initial conditions, mantle viscosity, and the link between time-dependent models and observations can be partially overcome with inverse models of mantle convection, as we demonstrate with a model tailored to the evolution of North America since the Late Cretaceous.

Our models use seismic tomography that resolves the remnants of Farallon plate subduction since the Mesozoic (*4*–*6*) as input for defining present-day structure (*7*). We invert mantle convection with the adjoint method that constrains the initial condition iteratively (*8*–*10*). Plate motions (*11*) are imposed as kinematic boundary conditions allowing the mapping between dynamic topography and stratigraphic observations (*12*). Because the temporal evolution of surface dynamic topography is related to poorly known mantle buoyancy and viscosity (*9*), we constrain these uncertainties with stratigraphic data, including reconstructions of paleoshorelines (*13*), sediment isopachs (*14*), and borehole tectonic subsidence (*15*, *16*).

A standard model of mantle convection (*17*) generates a first guess of the initial condition with a simple backward integration from the present to the past by reversing the sign of gravity, during which the Farallon slab remnants rise (instead of sink) (Fig. 1A). By 70 million years ago (Ma), within the upper mantle, the cold mantle diverges and partly deflects toward the east as a result of the reversely imposed plate motions (Fig. 1A), yielding a geophysically unreasonable subduction configuration. This cannot be overcome either by varying the radial viscosity structure or by performing additional forward-adjoint iterations, and such models are inconsistent with the temporal sequence of subsidence and uplift of the western interior (*18*, *19*). Essentially, the present Farallon seismic anomaly is too far to the east to be simply connected to the Farallon-North American boundary in the Mesozoic, a result implicit in forward models (*20*).

When we incorporate a simple parameterized stress guide (*21*) beneath the North American plate, the cold material becomes preferentially attached to the Farallon plate. Through adjoint iterations, the position and structure of the slab further adjust to reasonable subduction geometries (Fig. 1B). The stress guide strongly influences slab motion horizontally in the upper mantle, whereas lower mantle flow is less affected (Fig. 1, A and B). As the cold slab material rises in a backward sense, the upper part of the slab moves faster horizontally toward the trench than the lower part, and this leads to the formation of a flat- to shallow-dipping slab around 70 Ma extending 2000 km inland from the trench (Fig. 1B).

For a given density, the timing and extent of the flat slab formation depend on mantle viscosities, especially lower mantle viscosity, because the slab has a longer path in the lower compared to the upper mantle. The surface dynamic topography associated with the descending slab causes the continent to subside dynamically (*18*, *19*) and results in marine deposition, if below sea level. In practice, we assume that the sedimentation rate was constant and sea level eustatic while isostatically adjusting basin depth after each time step of 1 million years. The observed extent of Cretaceous flooding (Fig. 2A) (*14*, *22*), therefore, provides direct constraint on mantle viscosity. In a backward sense, a high viscosity ($3 \times 10^{22}$ Pa s) lower mantle causes the slab to rise slowly, reach the surface closer to the trench, and form a small area of flat slab subduction; the associated dynamic subsidence causes flooding with a smaller wavelength over shorter duration than observed (Fig. 2B). Alternatively, a mantle of smaller viscosity causes the slab to rise faster and reach the surface farther from the trench while forming a larger area of flat slab subduction, which causes extensive flooding spatially and temporally (Fig. 2C). A good fit to observed flooding is obtained if we decrease the lower mantle viscosity from the case in Fig. 2B by a factor of two to $1.5 \times 10^{22}$ Pa s (Fig. 2D). Tectonic subsidence extracted from boreholes reflects the magnitude and duration of surface subsidence for points fixed relative to the continent, and it is controlled by both the effective temperature and mantle rheology. Observed flooding and borehole subsidence jointly constrain the amplitude of the temperature anomaly, which, if too large, overpredicts either flooding or tectonic subsidence or

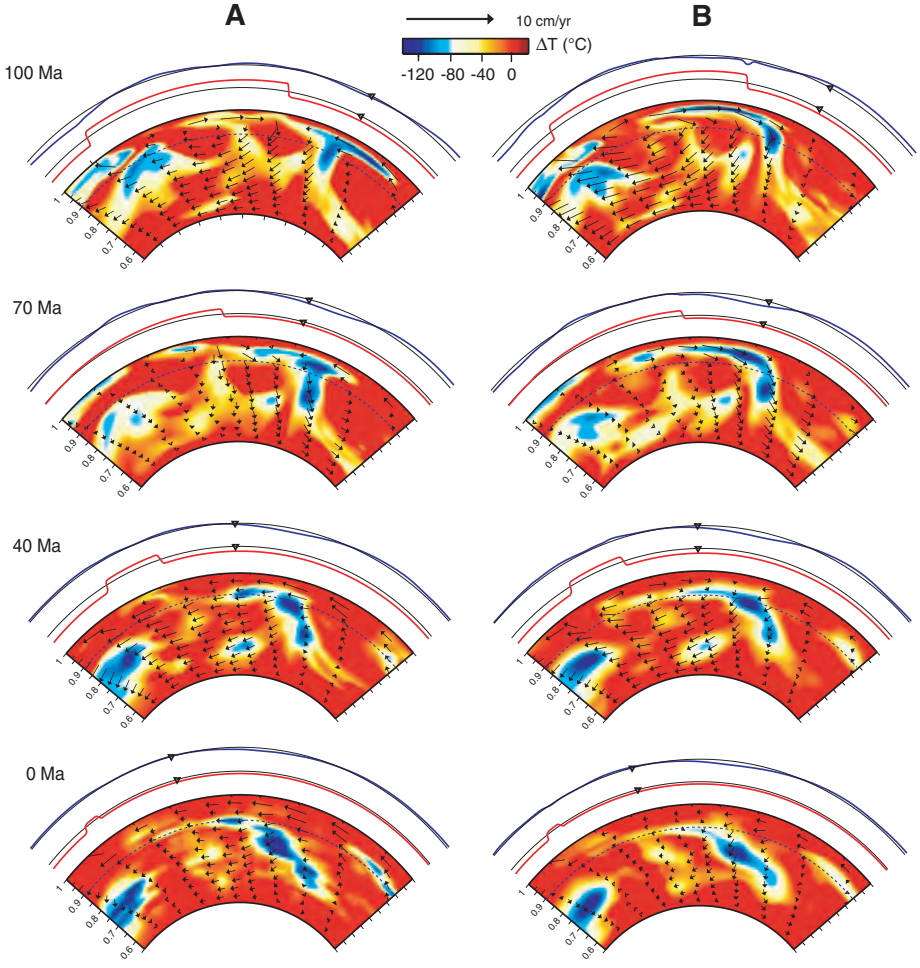


**Fig. 1.** (**A**) Temporal evolution of the Farallon slab during the simple backward integration at latitude 41°N with a standard model (*17*), where the lower:upper mantle viscosity is 15:1 (relative to $10^{21}$ Pa s) and the maximum effective temperature anomaly is 160°C. (**B**) Same as (A) but for a forward model based on the initial condition recovered with the adjoint method incorporating a stress guide (*21*). Cross sections show temperature anomalies, velocity vectors (in the forward sense), dynamic topography (blue) and longitudinal component of plate motion (red, positive is eastward) along this profile. The black triangles indicate the position of a borehole site (41.6°N, 254°E) about 250 km north of Denver. The dashed blue line marks upper-lower mantle interface. At 0 Ma, the left panel is seismic tomography, but the right is the prediction of tomography based on the forward-adjoint looping.

Seismological Laboratory, California Institute of Technology, Pasadena, CA 91125, USA.

*To whom correspondence should be addressed. E-mail: lijun@gps.caltech.edu

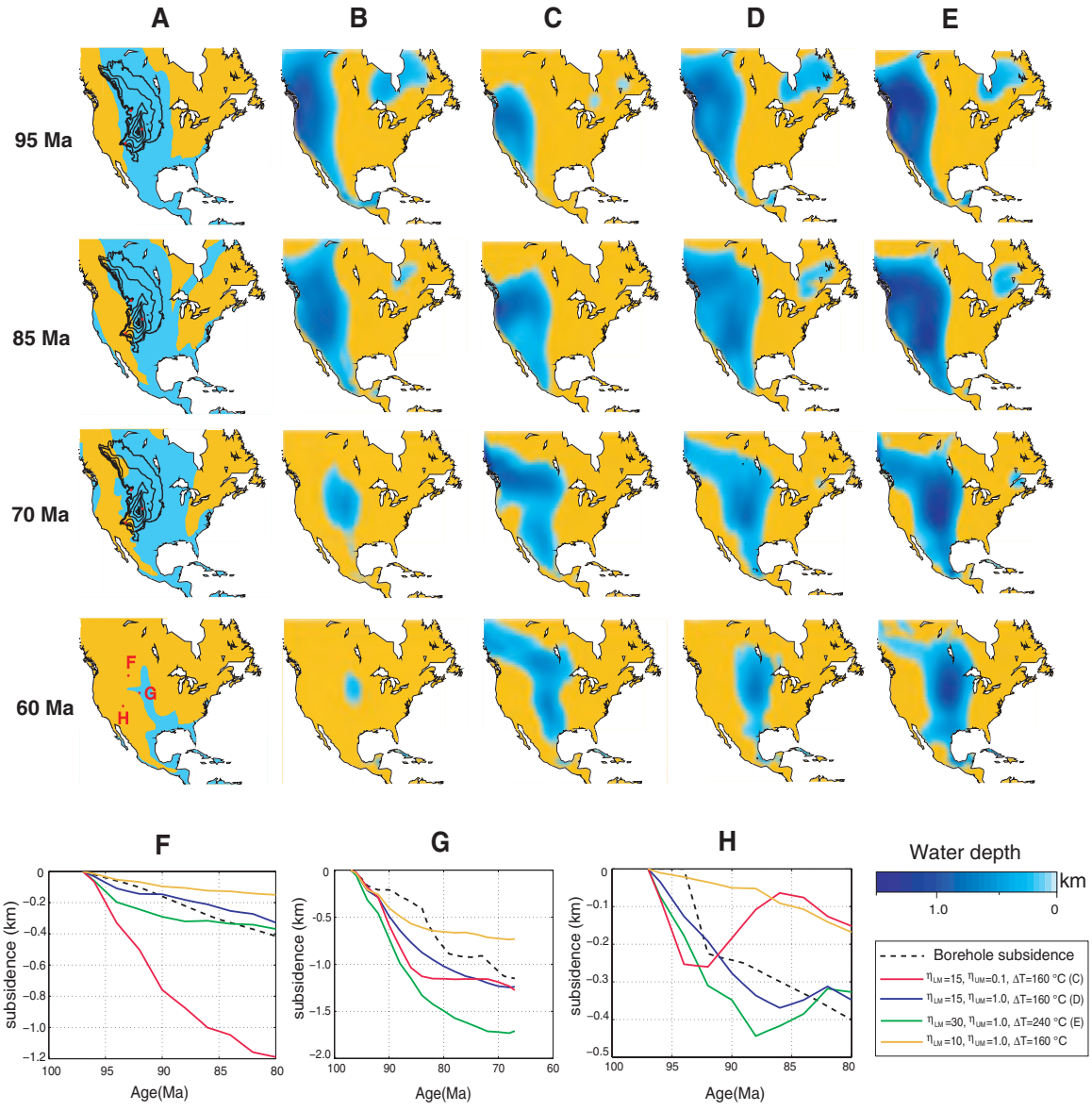


**Fig. 2.** Observed and predicted continental flooding and borehole subsidence for different temperature scaling and mantle viscosities. (**A**) Geologically inferred flooding (blue areas) bounded by paleoshorelines (*13*) with cumulative Cretaceous isopachs (*14*) overlain (2-km contour interval), with red dots indicating the three boreholes shown in (F) to (H). (**B** to **E**) Predicted flooding with lower-mantle viscosity $\eta_{LM}$ = 30, 15, 30 and upper-mantle viscosity $\eta_{UM}$ = 1, 0.1, 1, 1, respectively (relative to $10^{21}$ Pa s); cases (B) to (D) all have an effective temperature magnitude $\Delta T$ = 160°C, and (E) has $\Delta T$ = 240°C, where (D) is the best-fit model. (**F** to **H**) Observed and predicted borehole dynamic subsidence from four different models.

both (Fig. 2, E to H). An unreasonably small temperature anomaly does not reproduce as widespread flooding as observed (Fig. 2A). Borehole subsidence rate is inversely proportional to the upper mantle viscosity (*9*), and models constrained with such data show that decreasing upper mantle viscosity increases the rate of tectonic subsidence (Fig. 2, G and H). The phase of the borehole subsidence is another constraint: With data from three boreholes about 1000 km (north-south) and 800 km (east-west) apart, we can constrain the shape and position of the Farallon slab.

Our preferred model (Fig. 2D), which fits both flooding and borehole subsidence simultaneously, has a lower mantle viscosity of 1.5 × $10^{22}$ Pa s, an upper mantle viscosity of 1 × $10^{21}$ Pa s, and a present-day effective temperature (*21*) anomaly of 160°C. The correlation of water depth and dynamic topography with sediment isopachs (Fig. 2A) is used to further qualitatively validate the inversions. The inferred viscosities fall within bounds obtained with postglacial rebound (*23*), providing confirmation of the method. Given the simplicity of our model that has a three-layer viscosity mantle, limited spatial resolution of seismic tomography, and uncertainties in plate tectonic reconstructions, the inferred mantle properties are subject to further refinement.

Our preferred model depicts the evolution of the Farallon subduction from its early stage and includes an episode of flattening (Fig. 3). At 100 Ma, the slab is shallow-dipping, but not flat-lying (Fig. 3A). Slab flattening starts at about 90 Ma progressively from the trench and is characterized by a patch of thickened oceanic lithosphere about 1000 km wide that subducts to the northeast (Fig. 3B). The model predicts that this segment of the Farallon slab evolved into an isolated and thickened patch of oceanic lithosphere bounded by a series of shallow- to steep-dipping fragments (Fig. 3D). This configuration is sustained throughout the Late Cretaceous, accompanying a vast inland migration of the whole slab. In the model, the flat-lying slab sinks vertically from 70 Ma (Fig. 1B) (*21*). The inferred position of flat-lying subduction from the adjoint model correlates well with the region of basement-cutting Laramide-type faults in the western United States from 80 to 65 Ma (*24*). Our best model matches the along-strike extent of the faulting and its maximum in board extent (Fig. 3, B to D). However, both the onset and demise of flat subduction occur 10 million years earlier in the model compared with geological data. We made no attempt to tune model parameters based on the geologically inferred position of flat subduction. A present-day analog is the South American flat subduction in Peru, with its proposed linkage to subduction of an oceanic plateau (*25*). The morphology of the flat slab in our model (Fig. 3) may be consistent with a plateau subduction (*26*), showing a patch that is thicker and shallower than surrounding slab segments (Fig. 3).

Our inversion reverses subduction to only ~100 Ma, but even at that time, a shallow-dipping segment is intruding beneath the conti-

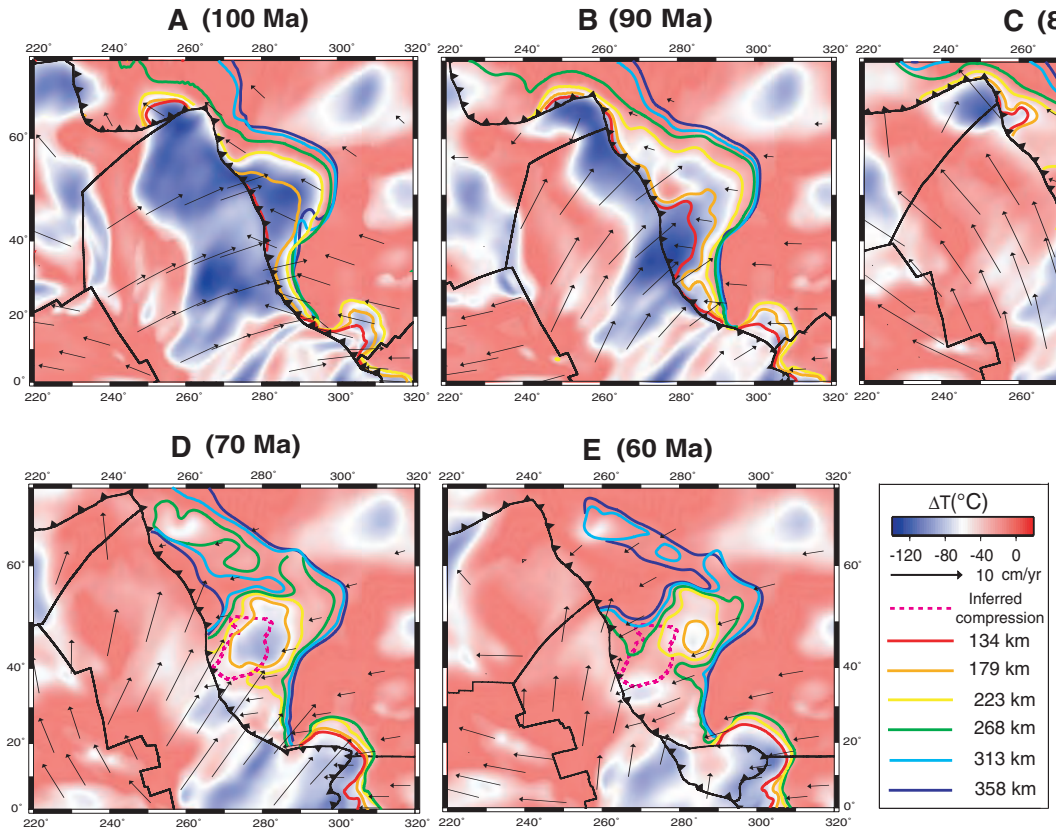


**Fig. 3.** Map view evolution of the Farallon subduction from the Late Cretaceous (**A** to **D**) to the Early Tertiary (**E**). The background temperature is at a depth of 223 km, and velocity vectors indicate imposed plate motions. The color lines (isotherms for a temperature of 30°C lower than ambient mantle) indicate the upper boundary of the slab at different depths with a warm (cold) color representing a small (large) depth. The dashed pink contour outlines the geologically inferred surface compression area occurring between 80 and 65 Ma (*24*).

nent (Fig. 3A). Consequently, because the inversion goes back to the period of anomalous subduction but no earlier, the conditions that gave rise to the flat-lying subduction cannot be recovered. Essentially, it is the present-day mantle structure that returns the flat-lying slab, as is evident from the predicted three-dimensional evolution of the Farallon plate subduction (*21*).

The adjoint models suggest that a vast zone of shallow-dipping subduction extended more than 1000 km eastward and northward from the zone of flat-lying subduction, especially from 90 to 70 Ma (Fig. 3, B to D). The zone is larger than inferred from a simplified set of forward models that neither incorporated the details of subduction nor attempted to match stratigraphy (*20*). The region of dynamic subsidence for North America, previously thought to be confined to portions of the western United States (*18*, *19*), was likely substantially larger in extent and mostly characterized by a Cenozoic unconformity (*19*). This relation is consistent with earlier suggestions that changes in dynamic topography should be reflected by unconformities (*19*). Much of the Canadian shield is sediment free, and the region has not been used to constrain dynamic models, but recent low-temperature thermochronology for basement samples in Northern Saskatchewan are consistent with 1 km of sediment burial and unroofing during the Cretaceous (*27*). This suggests that there is substantial ability to infer tectonic events when an adjoint of the convection problem is applied to seismic and plate motion data.

### References and Notes


1. G. Schubert, D. L. Turcotte, P. Olson, in *Mantle Convection in the Earth and Planets* (Cambridge Univ. Press, Cambridge, 2001), pp. 417–498.
2. G. F. Davies, in *Dynamic Earth: Plates Plumes and Mantle Convection* (Cambridge Univ. Press, Cambridge, 1999), pp. 262–323.
3. S. Zhong, M. Gurnis, *Science* **267**, 838 (1995).
4. S. P. Grand, *Philos. Trans. R. Soc. London A* **360**, 2475 (2002).
5. R. D. Van der Hilst, S. Widiyantoro, E. R. Engdahl, *Nature* **386**, 578 (1997).
6. Y. Ren, E. Stutzmann, R. D. Van der Hilst, J. Besse, *J. Geophys. Res.* **112**, B01302 (2007).
7. Both shear (*4*) and compressional (*5*, *6*) wave tomography show a prominent positive slablike seismic anomaly at mid-mantle depths below the east coast of North America. The high-velocity component of the shear wave seismic tomography (*4*) is converted to effective temperature (*21*) with a scaling factor of $2 \times 10^3$ °C km$^{-1}$ s. The upper 250-km signal associated with the North American craton is removed because it is likely neutrally buoyant (*28*). We also remove structures below 2400-km depth, where there is a clear gap in the tomographic image. For the rest, we assume a constant seismic-to-temperature scaling that we constrain by fitting our models to stratigraphic data.
8. H.-P. Bunge, C. R. Hagelberg, B. J. Travis, *Geophys. J. Int.* **152**, 280 (2003).
9. L. Liu, M. Gurnis, *J. Geophys. Res.* **113**, B08405 (2008).
10. The adjoint method, a gradient-based inversion, optimizes the initial condition by minimizing the mismatch between a model prediction and observation. For the nonlinear mantle convection, the observational constraint is seismic tomography. A simple backward integration of present-day mantle structures to the initial time provides a first-order estimate of the initial condition (*9*). In a forward-adjoint looping scheme, the forward run—which solves for conservation of mass ($u_{i,i} = 0$, where $u$ is velocity), momentum $[-P_{,i} + (\eta u_{i,j} + \eta u_{j,i})_{,j} + \rho_o \alpha \Delta T g \delta_{ir} = 0$, where $P$ is dynamic pressure, $\eta$ viscosity, $\Delta T$ effective temperature, $\alpha$ thermal expansion, $\rho_o$ reference density, and $g$ gravitational acceleration], and energy ($T_{,t} + u_i T_{,i} = \kappa T_{,ii}$, where $T$ is temperature, $t$ time, and $\kappa$ thermal diffusivity) for an incompressible Newtonian fluid—predicts the present-day mantle thermal structure, whereas the adjoint run, which solves for the kinematic adjoint equation ($\lambda_{,t} + u_i \lambda_{,i} + \kappa \lambda_{,ii} = 0$, where $\lambda$ is adjoint temperature) with $u$ stored from the forward run—back-propagates the mismatch to the initial time. The past mantle thermal state is iteratively updated until the mismatch with the observation (tomography) is small. The adjoint method has been incorporated (*9*) in a finite-element incompressible model of mantle convection (*17*).
11. We use GPlates reconstructions of global plate motions at 1-million-year intervals, in which the plate margins continuously evolve with self-consistent velocities between the plates and plate margins (*29*). The rotation poles of (*30*) are used in the GPlates reconstructions, implemented in a moving hotspot reference frame.
12. M. Gurnis, R. D. Müller, L. Moresi, *Science* **279**, 1499 (1998).
13. A. G. Smith, D. G. Smith, B. M. Funnel, *Atlas of Mesozoic and Cenozoic Coastlines* (Cambridge Univ. Press, Cambridge, 1994).
14. T. D. Cook, A. W. Bally, *Stratigraphic Atlas of North and Central America* (Princeton, Univ. Press, Princeton, NJ, 1975).
15. M. Pang, D. Nummedal, *Geology* **23**, 173 (1995).
16. S. Liu, D. Nummedal, P.-G. Yin, H.-J. Luo, *Basin Res.* **17**, 487 (2005).
17. We use CitcomS, a finite-element model (*31*) on a global mesh with a 129-by-129-by-65 grid on each of the 12 caps. We assume a free slip and isothermal core-mantle boundary and an isothermal surface. A Rayleigh number

(based on thickness of the mantle) of $9.4 \times 10^6$ is used (*21*). The three-layer viscosity includes a lithosphere with constant $5 \times 10^{22}$ Pa s viscosity, an upper mantle, and a lower mantle with varying viscosities to be constrained. Laterally, viscosity increases exponentially by one order of magnitude for a temperature drop of 200°C.
18. J. X. Mitrovica, C. Beaumont, G. T. Jarvis, *Tectonics* **8**, 1079 (1989).
19. P. M. Burgess, M. Gurnis, L. Moresi, *Bull. Geol. Soc. Am.* **109**, 1515 (1997).
20. H.-P. Bunge, S. P. Grand, *Nature* **405**, 337 (2000).
21. Materials and methods are available as supporting material on *Science* Online.
22. G. A. Bond, *Geology* **4**, 557 (1976).
23. G. A. Milne *et al.*, *J. Geophys. Res.* **109**, B02412 (2004).
24. J. Saleeby, *Bull. Geol. Soc. Am.* **115**, 655 (2003).
25. M.-A. Gutscher, W. Spakman, H. Bijwaard, E. R. Engdahl, *Tectonics* **19**, 814 (2000).
26. R. F. Livaccari, K. Burke, A. M. C. Sengor, *Nature* **289**, 276 (1981).
27. R. M. Flowers, *Eos* **52**, abstr. V34C-06 (2007).
28. S. Goes, S. van der Lee, *J. Geophys. Res.* **107**, 2050 (2002).
29. M. Gurnis *et al.*, *Eos* **52**, abstr. DI14A-07 (2007).
30. R. D. Müller *et al.*, *Geochem. Geophys. Geosys.* **9**, 10.1029/2007GC001743 (2008).
31. S. Zhong, M. T. Zuber, L. Moresi, M. Gurnis, *J. Geophys. Res.* **105**, 11,063 (2000).
32. This is contribution no. TO 88 of the Caltech Tectonics Observatory. The work was partially supported by the Gordon and Betty Moore Foundation through the Tectonics Observatory and the NSF through EAR-0609707. We appreciate discussions with J. Saleeby and R. D. Müller. The original CitcomS software was obtained from the Computational Infrastructure for Geodynamics (CIG) (http://geodynamics.org).

**Supporting Online Material**
www.sciencemag.org/cgi/content/full/322/5903/934/DC1
Materials and Methods
Figs. S1 to S3
References

8 July 2008; accepted 8 October 2008
10.1126/science.1162921

# Lack of Exposed Ice Inside Lunar South Pole Shackleton Crater

**Junichi Haruyama,[1] Makiko Ohtake,[1] Tsuneo Matsunaga,[2] Tomokatsu Morota,[1] Chikatoshi Honda,[1] Yasuhiro Yokota,[1] Carle M. Pieters,[3] Seiichi Hara,[4] Kazuyuki Hioki,[4] Kazuto Saiki,[5] Hideaki Miyamoto,[6] Akira Iwasaki,[7] Masanao Abe,[1] Yoshiko Ogawa,[2] Hiroshi Takeda,[8] Motomaro Shirao,[9] Atsushi Yamaji,[10] Jean-Luc Josset[11]**

The inside of Shackleton Crater at the lunar south pole is permanently shadowed; it has been inferred to hold water-ice deposits. The Terrain Camera (TC), a 10-meter-resolution stereo camera onboard the Selenological and Engineering Explorer (SELENE) spacecraft, succeeded in imaging the inside of the crater, which was faintly lit by sunlight scattered from the upper inner wall near the rim. The estimated temperature of the crater floor, based on the crater shape model derived from the TC data, is less than ~90 kelvin, cold enough to hold water-ice. However, at the TC's spatial resolution, the derived albedo indicates that exposed relatively pure water-ice deposits are not on the crater floor. Water-ice may be disseminated and mixed with soil over a small percentage of the area or may not exist at all.

Whether or not an amount of concentrated hydrogen on the lunar poles (*1*) forms water-ice is both a scientifically intriguing issue and a potentially important research subject in order for humans to settle on the Moon and travel further into space. Possible reservoirs of hydrogen on the lunar poles are permanently shadowed areas (PSAs), which receive no direct sunlight and are extremely cold (*2*, *3*). Because the present rotation inclination of the Moon is nearly zero (~1.5° from normal to the ecliptic plane), topographic lows on the lunar poles become PSAs. Shackleton Crater, which lies at the lunar south pole, has therefore been considered as a possible water-ice reservoir in its PSA. Bistatic radar observations made by the Clementine probe (*4*, *5*) implied that there are water-ice deposits inside Shackleton Crater. However, subsequent Earth-based radar observations showed little evidence for the existence of water-ice deposits (*6*), although they could observe only an upper part of the inner wall of Shackleton.

We investigated the interior of Shackleton Crater with the panchromatic Terrain Camera (TC), a 10-m-resolution stereo camera onboard the Selenological and Engineering Explorer (SELENE) spacecraft (also nicknamed Kaguya) (*7*). The method of our observation was based on the idea that the PSA is weakly lit by sunlight scattered from nearby higher terrains. The small lunar rotation inclination means that the maximum scattering illumination occurs during the lunar mid-summer. The first lunar south pole summer after the SELENE launch in September 2007 was during October to December 2007. Clear images of inside of Shackleton Crater were first acquired on 19 November 2007 (Fig. 1, A and B), from which we also produced a digital terrain model (DTM) (Fig. 1, C and D). Shackleton Crater is a truncated cone-shaped crater and has an almost concentric circular rim with a radius of ~10.5 km, a floor with a radius of ~3.3 km, and a depth of ~4.2 km; it is much deeper than other similarly sized lunar craters (*8*). Inside, the crater has an almost smooth but cratered inner wall. Two mounds are seen adjacent to the inner wall that are probably the result of landslides from the inner wall. A hill a few hundred meters in height occupies the crater center. A terrace structure is associated with the hill and is elongated toward the inner wall. It has a number of depressions that are probably craters.

The inner wall slopes ~30°, which is consistent with a result from the Earth-based radar observation of the upper portion of the Shackleton Crater inner wall that is opposite the Earth (*6*). The entire rim of Shackleton Crater is tilted ~1.5° toward a direction of 50° to ~90° from the Earth-side hemisphere. Thus, under the illumination conditions of the lunar summer, the solar elevation angle from the opposite-side rim occasionally becomes a maximum ~3.0° on a few days when the sub-solar point is ~70°E in longitude and ~1.5°S in latitude, such as on 19 November 2007. Meanwhile, when the sub-solar point becomes far from ~70°E in longitude, the illuminated areas on the inner wall of Shackleton decreases, and the floor remains in darkness. Similarly bright conditions occurred around 18 December 2007 as anticipated, and we obtained additional clear images of the crater interior then. After December 2007, the solar elevation angle decreased, and the inside of Shackleton was less lit. The next time the bottom of Shackleton Crater will be maximally lit will occur around 7 November 2008. Based on the observed shape parameters from the TC DTM, we were able to estimate the surface temperature of the PSA of the crater floor [see the supporting online material (SOM) text] (Fig. 1E). We assumed that the crater has a Lambert diffusive surface and the same albedo between the inner wall and the floor and that the solar elevation angle is 3.0° on the date of its most illuminated condition (for example, 19 November 2007), as in Fig. 1A. As is seen in Fig. 1E, the highest estimated temperature is ~88 K in the center of the floor. The floor temperature was largely determined by the radiation in the infrared range and not by that in the visible range. Thus, the shape parameters, particularly its depth, predominated because the infrared radiation in the crater rapidly decreases as its area increases. The surface visual albedos and scattering laws were almost negligible in estimating the temperature. The loss rate of any ice by vaporization at 90 K is approximately $10^{-26}$ to $10^{-27}$ m/s (*9*). Therefore, any water vapor brought here by comets or meteorites could have been trapped for billions of years.

However, we could not find any conspicuously bright areas in Shackleton Crater. The hemispherical visual albedo around the center of the crater

[1]Institute of Space and Astronautical Science, Japan Aerospace Exploration Agency, Sagamihara, Kanagawa 229-85105, Japan. [2]Center for Global Environmental Research, National Institute for Environmental Studies, Tsukuba, Ibaraki 305-8506, Japan. [3]Department of Geological Sciences, Brown University, Providence, RI 02912, USA. [4]NTT DATA CCS Corporation, Koto-ku, Tokyo 136-0071, Japan. [5]Department of Earth and Space Science, Graduate School of Science, Osaka University, Toyonaka, Osaka 560-0043, Japan. [6]University Museum, The University of Tokyo, Bunkyo-ku, Tokyo 113-0033, Japan. [7]Department of Aerospace and Astronautics, The University of Tokyo, Bunkyo-ku, Tokyo 113-8656, Japan. [8]Forum Research, Chiba Institute of Technology, Narashino, Chiba 275-0016, Japan. [9]Taito-ku, Tokyo 111-0035, Japan. [10]Division of Earth and Planetary Sciences, Kyoto University, Sakyo-ku, Kyoto 606-8502, Japan. [11]Space Exploration Institute, CP 774, CH-2002 Neuchatel, Switzerland.